Nanomechanical coupling between microwave and optical photons

Joerg Bochmann[†], Amit Vainsencher[†], David D. Awschalom and Andrew N. Cleland[*]

A variety of nanomechanical systems can now operate at the quantum limit[1–4], making quantum phenomena more accessible for applications and providing new opportunities for exploring the fundamentals of quantum physics. Such mechanical quantum devices offer compelling opportunities for quantum-enhanced sensing and quantum information[5–7]. Furthermore, mechanical modes provide a versatile quantum bus for coupling hybrid quantum systems, supporting a quantum-coherent connection between different physical degrees of freedom[8–13]. Here, we demonstrate a nanomechanical interface between optical photons and microwave electrical signals, using a piezoelectric optomechanical crystal. We achieve coherent signal transfer between itinerant microwave and optical fields by parametric electro-optical coupling using a localized phonon mode. We perform optical tomography of electrically injected mechanical states and observe coherent interactions between microwave, mechanical and optical modes, manifested as electromechanically induced optical transparency. Our on-chip approach merges integrated photonics with microwave nanomechanics and is fully compatible with superconducting quantum circuits, potentially enabling microwave-to-optical quantum state transfer, and photonic networks of superconducting quantum bits[14–16].

In engineered quantum systems, the interactions between different physical degrees of freedom can be strongly enhanced by mode confinement in nanoscale structures. In the field of optomechanics[17], this has recently enabled quantum-coherent coupling between optical and mechanical modes, and quantum control of mechanical motion[2–4]. The emerging possibility of mechanically mediated state transfer[11,18–22] promises a new type of quantum transducer, using nanomechanical motion to translate electrical or spin-based quantum states to photonic states, thereby creating an optical quantum interface.

Here, we present a nanomechanical transducer in which a purpose-designed microwave-frequency mechanical mode generates a coupling between electrical signals at 4 GHz and optical photons at 200 THz. Strong coherent interactions between the electrical, mechanical and optical modes are enabled by combining electromechanical and optomechanical coupling in a piezoelectric optomechanical crystal. Fabricated from aluminium nitride (AlN) and monolithically integrated on-chip, the transducer is fully compatible with superconducting quantum circuits and is well suited for cryogenic operation. Operating at microwave mechanical frequencies, this device in principle allows quantum ground-state control of the mechanical mode[1] and state transfer between quantum microwave and optical channels.

The transducer is illustrated in Fig. 1. A mechanically suspended beam of AlN ($0.33 \times 1 \times 100\ \mu m^3$) is patterned as an optomechanical crystal, designed to support a highly localized phonon mode

at 4.2 GHz and a co-localized optical mode at 196 THz with strong optomechanical coupling[3,23]. The beam also includes a pair of aluminium electrodes connected to an on-chip, broadband microwave transmission line, enabling strong electromechanical coupling through the piezoelectric effect in AlN (refs 1,24,25). The transducer is connected optically using an evanescently coupled rib waveguide, with signals routed to a pair of optical fibres by means of on-chip grating couplers. The optical design wavelength is 1,550 nm, matching a fibre-optic telecommunication band. The 4–5 GHz design frequency of the confined mechanical mode is compatible with the operating frequency of superconducting quantum bits[1,15,16].

The dynamics of the integrated system are described by the Hamiltonian of equation (1),

$$\hat{H} = \hbar\omega_{cav}\left(a^\dagger a + \frac{1}{2}\right) + \hbar\omega_m\left(b^\dagger b + \frac{1}{2}\right) + \hbar g_{om}a^\dagger a(b + b^\dagger) + \hbar g_{em}(b^\dagger c + bc^\dagger) \quad (1)$$

where the first term is the energy in the optical cavity mode, with photon operators $a(a^\dagger)$, the second term is the energy in the microwave-frequency mechanical mode, with phonon operators $b(b^\dagger)$, the third term is the usual optomechanical interaction term with optomechanical interaction strength g_{om} (refs 3,17), and the last term represents electrical actuation of the mechanical mode, using a Jaynes–Cummings interaction with coupling strength g_{em} and an electrical driving field with operators $c(c^\dagger)$ (refs 1,26).

We characterized the room-temperature optomechanical properties of the device using a tunable diode laser. The optical transmission signal, shown in Fig. 1d, exhibits a high-quality-factor photonic crystal resonance at 1,531.5 nm (intrinsic quality factor $Q_{opt} = 130{,}000$, optical linewidth $\kappa/2\pi = 2.5$ GHz) indicative of the confined optical mode shown in Fig. 1b.

For mechanical modes with sufficient overlap with the optical mode, thermomechanical motion of the photonic crystal induces phase and intensity modulations on the transmitted probe laser light, detected as resonances at the mechanical frequencies in the optical noise power spectrum. We observe several thermally excited flexural, torsional and extensional beam modes, shown in Fig. 2. The most relevant spectral feature is the resonance at $\omega_m/2\pi = 4.24$ GHz, induced by the mechanical breathing mode localized at the centre of the optomechanical crystal, shown in Fig. 2b (mechanical quality factor $Q_{mech} = 2{,}500$, linewidth $\Gamma_{mech}/2\pi = 1.7$ MHz). Probed in thermal equilibrium at room temperature ($N_{th} \approx 1{,}500$ phonons), the integral over the resonance in the noise spectral density yields an optomechanical coupling $g_{om}/2\pi = 30 \pm 5$ kHz, in agreement with numerical simulations (Supplementary Information). We note that the mechanical mode frequency ω_m is significantly larger than the optical linewidth κ,

Department of Physics, University of California, Santa Barbara, California 93106, USA. [†]These authors contributed equally to this work.
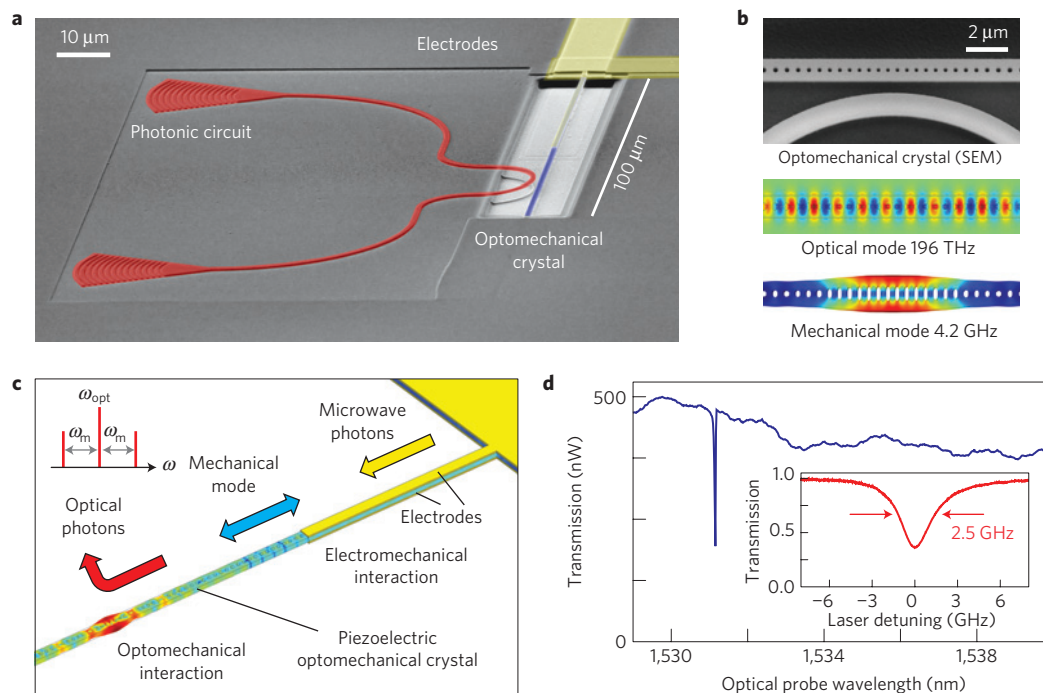*e-mail: anc@physics.ucsb.edu

Figure 1 | Device and electro-optomechanical coupling scheme. a, Scanning electron micrograph (SEM) of the device (angled view) showing the mechanically suspended AlN optomechanical crystal (blue) with aluminium electrodes (yellow) and the AlN photonic circuit (red, rib waveguide and grating couplers). **b**, Top view of the central region of the optomechanical crystal (SEM), and numerical simulations of the electrical field distribution of the optical mode at $\omega_{cav}/2\pi = 196$ THz and the mechanical displacement profile of the localized mechanical breathing mode at $\omega_m/2\pi = 4.2$ GHz. **c**, Schematic of electro-optomechanical transduction in the piezoelectric optomechanical crystal (light blue). An electrical microwave signal on the electrodes (yellow) induces strain by piezoelectric coupling and resonantly excites the engineered breathing mode of the optomechanical crystal. Parametric optomechanical coupling to the co-localized optical mode (not shown) generates optical sidebands on a probe laser field (schematic, top left) thereby upconverting the mechanical (electrical) state to optical frequencies. Colour coding of the suspended beam indicates mechanical displacement of the electrically driven device (numerical simulation). **d**, Measured optical transmission as a function of optical probe wavelength. The photonic crystal resonance at 1,531.5 nm has a linewidth $\kappa/2\pi = 2.5$ GHz full-width at half-maximum with resonant transmission $T = 37\%$ (inset).
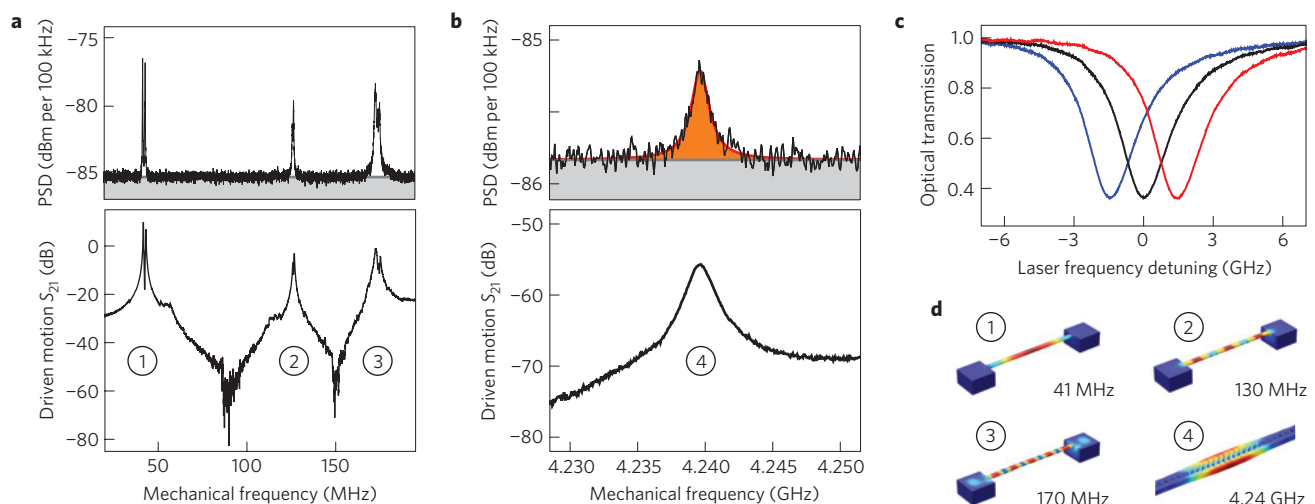

Figure 2 | Electro-optomechanical response and optically detected thermal and driven mechanical motion. a, Optically detected mechanical motion of the optomechanical crystal in the 20–200 MHz frequency range. Upper panel: thermomechanical motion detected in the optical noise power spectral density (PSD) at room temperature (technical noise floor indicated in grey). Lower panel: electrically driven electro-optomechanical response S_{21} (see text for details). Circled numbers indicate the extensional modes shown in **d**. **b**, Thermally excited (upper panel) and electrically driven (lower panel) localized breathing mode resonance at 4.24 GHz, with a mechanical linewidth $\Gamma_m/2\pi = 1.7$ MHz (full-width at half-maximum) and optomechanical coupling constant $g_{om}/2\pi = 30 \pm 5$ kHz. **c**, Piezoelectric tuning of the optomechanical crystal. Shown is the probe laser transmission for applied external voltages of $V_{dc} = (-5, 0, 5)$ V (blue, black, red lines). The cavity frequency shift is $d\omega_{cav}/dV_{dc} = 2\pi \times 310$ MHz V^{-1}. **d**, Identification and numerical simulation of mechanical modes. Each extensional mode resonance is split into multiplets by the presence of electrodes on the suspended beam, breaking the beam's inversion symmetry; one representative mode per multiplet is shown for clarity (drawing not to scale).
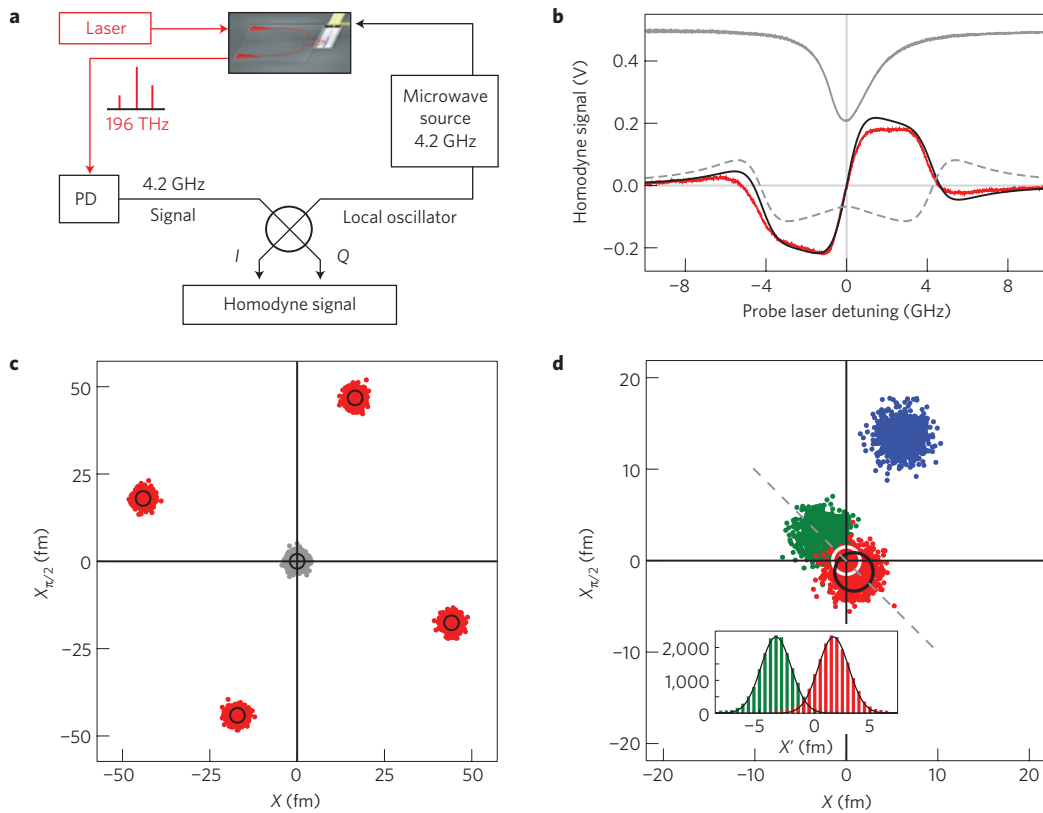
Figure 3 | Optical homodyne tomography of electrically injected mechanical states. a, Experiment schematic for homodyne detection. A 4.24 GHz microwave source electrically excites the mechanical breathing mode and provides the local oscillator signal. Mechanically induced optical sidebands at 4.24 GHz are photodetected (PD) and mixed (IQ) with the local oscillator. **b**, Measured homodyne signal (red) when sweeping the laser across the optical cavity resonance, with a comparison to theory for optomechanical phase modulation (black) and intensity modulation (dashed grey). The optical cavity transmission profile is shown for reference (solid grey). **c**, Measured quadrature distributions (red) of electrically excited mechanical states with mean phonon occupation $N_{exc} \approx 1{,}100$ at different injection phases ($0, \pi/2, \pi, 3\pi/2$; shown anticlockwise starting at the upper right). Detected phase angle is relative to the local oscillator. Black circles: $1/e$ width of measured probability distributions. Grey: homodyne detection with no electrical injection, representing the combined technical and thermal noise floor. **d**, Quadrature distributions of injected mechanical states with different phases and mean phonon occupations $N_{exc} \approx 100$ (blue), 7 (green) and 1 (red, black circle: $1/e$ width). White circle: expected amplitude of an injected one-phonon state, providing a scale for the impact of noise at the chosen measurement bandwidth of 200 Hz. Inset: histograms of $N_{exc} \approx 1$ and 7 distributions along a cross-section given by the dashed line; bin size is 0.5 fm. Gaussian fits (black) match the observed distributions.

meeting the crucial requirement for operation in the resolved sideband regime, and allowing access to the rich toolbox of cavity optomechanics[17]. These performance metrics, achieved using a strong piezoelectric material, provide an excellent outlook for quantum electro-optomechanics.

We use piezoelectric actuation of the optomechanical crystal to generate a strong optical response. When applying a fixed voltage difference V_{dc} to the electrodes (Fig. 2c), piezoelectric dilatation shifts the photonic crystal resonance frequency $\omega_{cav}/2\pi$ and we measure $d\omega_{cav}/dV_{dc} = 2\pi \times 310\,\text{MHz V}^{-1}$, in agreement with numerical simulations. The shift is linear and preserves the sign of the applied voltage, in contrast to capacitive actuation[27]. When applying radiofrequency electrical signals to the transducer electrodes, we induce a complex, frequency-dependent displacement field, generating a series of distinct electro-optomechanical resonances. Sweeping the electrical excitation frequency Ω while monitoring the mechanically induced optical sideband power at frequency $\omega_{laser} \pm \Omega$ yields the electro-optic transfer function $S_{21}(\Omega)$, shown in Fig. 2a,b (Supplementary Information). Comparison of this transfer function with the thermomechanical spectrum and numerical simulations allows us to identify the most prominent resonances (Fig. 2a,b,d). Resonances between 20 and 200 MHz correspond to electrically actuated in-plane extensional beam modes. The fundamental breathing mode of

the optomechanical crystal appears as a resonance at 4.24 GHz (Fig. 2b), with an effective electro-optomechanical frequency shift $d\omega_{cav}/dV_{rms} = 2\pi \times 300\,\text{MHz}/V_{rms}$. We focus on this mode for the remainder of this work.

A prerequisite for quantum state transfer is the faithful mapping of phase and amplitude from the electrical to the optical field through the mechanical mode. We investigate this by performing optical homodyne tomography of the electrically generated localized phonon state, shown schematically in Fig. 3a. We downconvert the optomechanically induced optical sidebands of the 196 THz optical carrier to 4.24 GHz through optical beat note detection, and further downconvert to a homodyne signal by quadrature-sensitive mixing with the radiofrequency drive signal (see Supplementary Information). Figure 3b shows the measured homodyne signal when exciting the breathing mode electromechanically at a frequency $\Omega_{exc} = \omega_m$ with $N_{exc} \approx 10^6$ phonons, while sweeping the laser frequency across the optical cavity resonance. The characteristic antisymmetry of the homodyne signal provides confirmation of frequency modulation, as expected for parametric optomechanical coupling, in contrast to intensity modulation (see Supplementary Information).

Homodyne tomography allows us to reconstruct the quadrature probability distributions of different mechanical states. We electrically inject classical mechanical states at $\Omega_{exc} = \omega_m$ with a mean
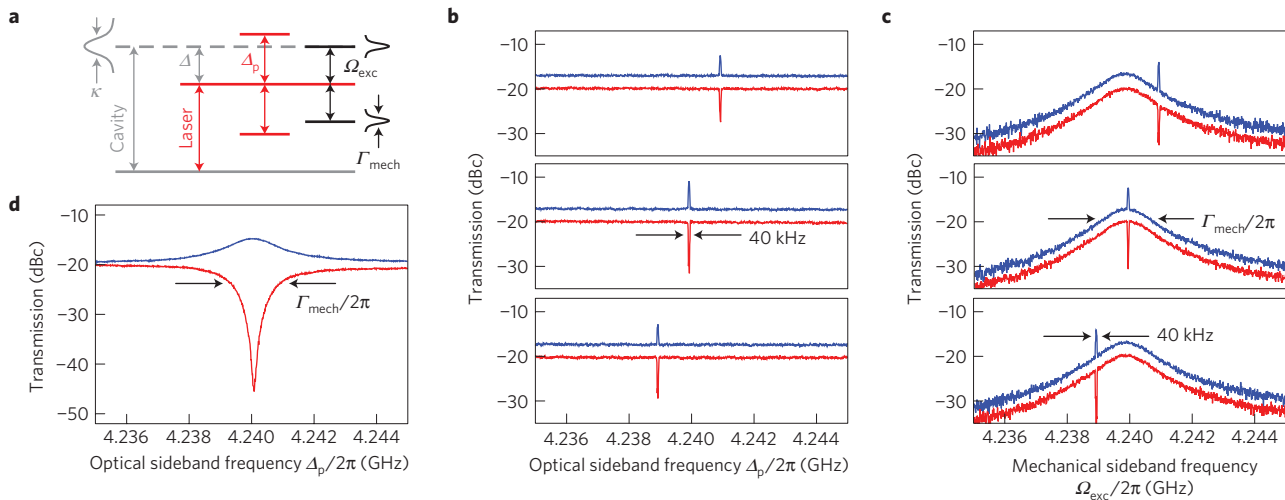
Figure 4 | Electro-optomechanically induced transparency. a, Schematic of relevant optical, electrical and mechanical frequencies and resonance widths. Δ is the laser detuning from cavity resonance; here, $\Delta = \omega_m$; Δ_p is the optical probe sideband frequency; Ω_{exc} is the mechanical drive frequency. Transparency occurs when the optical probe field and mechanically induced sideband are resonant, $\Delta_p = \Omega_{exc}$. **b**, Optical probe sideband transmission as a function of sideband frequency Δ_p for the mechanical resonator driven electrically at detuning $\Omega_{exc} - \Delta = 2\pi \times (-1, 0, 1)$ MHz (lower, middle, upper panel) from the mechanical breathing mode resonance, with the relative phase of the probe sideband and electromechanical sideband set to $\phi = \pi$ (red) and $\phi = 0$ (blue, offset vertically by 3 dB for clarity). The width of the transparency dip (peak) is 40 kHz, limited by the measurement bandwidth. **c**, Transmission of the electromechanically induced sideband for optical sideband frequencies $\Delta_p - \Delta = 2\pi \times (-1, 0, 1)$ MHz. The signal envelope is the mechanical susceptibility in the electro-optomechanical response. **d**, Optical sideband transmission when the probe and electromechanical excitation frequency are tuned across the mechanical resonance synchronously ($\Omega_{exc} = \Delta_p$), with relative phase $\phi = \pi$ (red) and $\phi = 0$ (blue), giving the envelope function of the transparency features in **b,c**.

phonon number $N_{exc} \approx 1,100$ at phases of 0, $\pi/2$, π and $3\pi/2$ with respect to the local oscillator, and obtain four distinct quadrature distributions (Fig. 3c), illustrating phase-preserving mapping from the electrical to the optical channel by way of the mechanical mode. The spread in the measured distributions reflects the combination of technical and thermal noise in the system. We then reduced the excitation signal to achieve on average $N_{exc} \approx 100$, 7 and 1 phonons (Fig. 3d). The successful detection of these few-phonon excitations on top of an incoherent thermal background of $N_{th} \approx 1,500$ phonons is aided by the narrow measurement bandwidth (200 Hz), yielding a detection noise floor comparable to the displacement amplitude of one phonon.

The coherent interaction of photons and phonons in cavity optomechanics manifests itself through the phenomenon of optomechanically induced transparency[28,29] (OMIT). With the phonon mode coupled to an electrical mode, we expect a similarly striking effect in the electrically driven optical response: electro-optomechanically induced transparency. We add optical probe sidebands at frequencies $\omega_p = \omega_{laser} \pm \Delta_p$ to the optical carrier signal at ω_{laser} and monitor the sideband transmission through the device. The laser carrier is red-detuned from the cavity resonance by the breathing mode frequency ($\omega_{cav} - \omega_{laser} = \Delta = \omega_m = 2\pi \times 4.24$ GHz), and the mechanical breathing mode is driven electrically at frequency Ω_{exc}. This situation is similar to OMIT, except the mechanical motion is driven electrically instead of optically, and we control the mechanical phase, amplitude and frequency independently. The measured optical sideband transmission signals are shown in Fig. 4. A theoretical analysis is given in the Supplementary Information.

When scanning the optical sideband frequency Δ_p across the cavity resonance (at fixed Ω_{exc}), we observe a narrow transparency dip in the sideband transmission (Fig. 4b). As in OMIT, this occurs when $\Delta_p = \Omega_{exc}$, and is caused by destructive interference between the electromechanical and optical excitation paths of the coupled system. However, when the phase of the

electrical excitation signal and hence the mechanical motion is changed by π, the sideband transmission exhibits a peak as the interference becomes constructive. In contrast to OMIT, this mechanical phase is an externally controlled parameter, and the width of the transparency window is limited only by the measurement bandwidth, which can be much narrower than the mechanical linewidth. This is exemplified when the electromechanical excitation frequency Ω_{exc} is swept while keeping the optical sideband fixed at Δ_p (Fig. 4c). The Lorentzian envelope of the mechanical sideband transmission is given by the mechanical susceptibility of the system, and the characteristic transparency again occurs at $\Delta_p = \Omega_{exc}$. The envelope function of all possible transparency dips (peaks) is measured by synchronously sweeping the probe sideband Δ_p and mechanical drive frequency Ω_{exc} (Fig. 4d), giving extinction ratios as high as 25 dB in the transparency window.

The controlled interactions between electrical signals, phonons and optical photons realized in this device provide an excellent outlook for quantum electro-optomechanics. The mechanical frequency of more than 4 GHz gives access to the single quantum regime at temperatures below about 0.3 K, and is well suited for integration into a superconducting quantum bit architecture. From the transducer geometry and extrapolation from previous work[1], we can expect electromechanical coupling rates up to $g_{em}/2\pi = 40$ MHz when coupled to a single superconducting qubit[1], exceeding the expected qubit decoherence rate $\gamma/2\pi < 1$ MHz. Operating in the resolved-sideband regime of optomechanics, the measured optomechanical coupling of $g_{om}/2\pi = 30$ kHz should enable mechanical-to-optical quantum swap operations at a rate $\Omega_{om}/2\pi = 6$ MHz at moderate laser power, faster than the intrinsic decoherence rate of the mechanical resonator $\Gamma/2\pi = 1.7$ MHz (Supplementary Information). Our transducer concept thus opens a potentially viable path towards microwave-to-optical quantum state transfer. This should allow mapping of on-chip synthesized microwave quantum states[30] to optical modes, thereby providing

a unique source of non-classical light and enabling long-range quantum networks of superconducting quantum circuits.

References

1. O'Connell, A. D. *et al.* Quantum ground state and single phonon control of a mechanical resonator. *Nature* **464,** 697–703 (2010).
2. Teufel, J. D. *et al.* Sideband cooling of micromechanical motion to the quantum ground state. *Nature* **475,** 359–363 (2011).
3. Chan, J. *et al.* Laser cooling of a nanomechanical oscillator into its quantum ground state. *Nature* **478,** 89–92 (2011).
4. Verhagen, E., Deleglise, S., Weis, S., Schliesser, A. & Kippenberg, T. J. Quantum-coherent coupling of a mechanical oscillator to an optical cavity mode. *Nature* **482,** 63–67 (2012).
5. Stannigel, K. *et al.* Optomechanical quantum information processing with photons and phonons. *Phys. Rev. Lett.* **109,** 013603 (2012).
6. Palomaki, T. A., Harlow, J. W., Teufel, J. D., Simmonds, R. W. & Lehnert, K. W. Coherent state transfer between itinerant microwave fields and a mechanical oscillator. *Nature* **495,** 210–214 (2013).
7. The LIGO Scientific Collaboration, A gravitational wave observatory operating beyond the quantum shot-noise limit. *Nature Phys.* **7,** 962–965 (2011).
8. Rabl, P. *et al.* A quantum spin transducer based on nanoelectromechanical resonator arrays. *Nature Phys.* **6,** 602–608 (2010).
9. Kolkowitz, S. *et al.* Coherent sensing of a mechanical resonator with a single-spin qubit. *Science* **335,** 1603–1606 (2012).
10. Camerer, S. *et al.* Realization of an optomechanical interface between ultracold atoms and a membrane. *Phys. Rev. Lett.* **107,** 223001 (2011).
11. Hill, J. T., Safavi-Naeini, A. H., Chan, J. & Painter, O. Coherent optical wavelength conversion via cavity optomechanics. *Nature Commun.* **3,** 1196 (2012).
12. Arcizet, O. *et al.* A single nitrogen-vacancy defect coupled to a nanomechanical oscillator. *Nature Phys.* **7,** 879–883 (2011).
13. Cirac, J. I. & Zoller, P. Quantum computations with cold trapped ions. *Phys. Rev. Lett.* **74,** 4091–4094 (1995).
14. Ritter, S. *et al.* An elementary quantum network of single atoms in optical cavities. *Nature* **484,** 195–200 (2012).
15. Mariantoni, M. *et al.* Implementing the quantum von Neumann architecture with superconducting circuits. *Science* **334,** 61–65 (2011).
16. Lucero, E. *et al.* Computing prime factors with a Josephson phase qubit quantum processor. *Nature Phys.* **8,** 719–723 (2012).
17. Aspelmeyer, M., Kippenberg, T. J. & Marquardt, F. Cavity optomechanics. Preprint at http://arxiv.org/abs/1303.0733 (2013).
18. Tian, L. Adiabatic state conversion and pulse transmission in optomechanical systems. *Phys. Rev. Lett.* **108,** 153604 (2012).
19. Wang, Y-D. & Clerk, A. A. Using interference for high fidelity quantum state transfer in optomechanics. *Phys. Rev. Lett.* **108,** 153603 (2012).
20. Dong, C., Fiore, V., Kuzyk, M. & Wang, H. Optomechanical dark mode. *Science* **338,** 1609–1613.
21. Safavi-Naeini, A. H. & Painter, O. Proposal for an optomechanical traveling wave phonon-photon translator. *New J. Phys.* **13,** 013017 (2011).
22. Regal, C. A. & Lehnert, K. W. From cavity electromechanics to cavity optomechanics. *J. Phys. Conf. Ser.* **264,** 012025 (2011).
23. Eichenfield, M., Chan, J., Camacho, R. M., Vahala, K. J. & Painter, O. Optomechanical crystals. *Nature* **462,** 78–82 (2009).
24. Xiong, C. *et al.* Aluminum nitride as a new material for chip-scale optomechanics and nonlinear optics. *New J. Phys.* **14,** 095014 (2012).
25. Xiong, C. *et al.* Cavity piezooptomechanics: Piezoelectrically excited, optically transduced optomechanical resonators. *Appl. Phys. Lett.* **102,** 021110 (2013).
26. Cleland, A. N. & Geller, M. R. Superconducting qubit storage and entanglement with nanomechanical resonators. *Phys. Rev. Lett.* **93,** 070501 (2004).
27. Winger, M. *et al.* A chip-scale integrated cavity-electro-optomechanics platform. *Opt. Express* **19,** 24905–24921 (2011).
28. Weis, S. *et al.* Optomechanically induced transparency. *Science* **330,** 1520–1523 (2010).
29. Safavi-Naeini, A. H. *et al.* Electromagnetically induced transparency and slow light with optomechanics. *Nature* **472,** 69–73 (2011).
30. Hofheinz, M. *et al.* Synthesizing arbitrary quantum states in a superconducting resonator. *Nature* **459,** 546–549 (2009).

Acknowledgements

Author contributions

J.B. and A.V. fabricated the sample, performed experiments and analysed data. All authors contributed to developing the concept of the experiment and manuscript preparation.

Additional information

Supplementary information is available in the online version of the paper. Reprints and permissions information is available online at www.nature.com/reprints. Correspondence and requests for materials should be addressed to A.N.C.

Competing financial interests

The authors declare no competing financial interests.